Nanoscale Advances

ROYAL SOCIETY OF CHEMISTRY

PAPER

View Article Online
View Journal

Cite this: DOI: 10.1039/d5na01105a

First principles simulations of transition metals for diodes: challenges and approaches to overcome inaccuracies in calculations

Marina Petroselli,[a] Elaheh Mohebbi,[a] Eleonora Pavoni,[a] Pierluigi Stipa,[a] Davide Mencarelli,[b] Emiliano Laudadio *[a] and Luca Pierantoni[b]

Received 29th November 2025
Accepted 6th April 2026

DOI: 10.1039/d5na01105a

rsc.li/nanoscale-advances

The electronic, optical, and mechanical properties of transition metals belonging to groups 4B (Cr, Mo, and W), 8B (Ni, Pd, and Pt), and 9B (Cu, Ag, and Au) were investigated using Density Functional Theory (DFT). Three exchange–correlation functionals PBE, R^{2}SCAN, and HSE06 were used and compared to evaluate their capability in prediction performance based on different physical properties. The results obtained from the density of states (DOS) calculations revealed a strong agreement between PBE and R^{2}SCAN, while HSE06 introduced significant shifts in the valence and conduction regions due to the inclusion of the exact Hartree–Fock exchange. The optical properties of these metals highlighted that PBE and R^{2}SCAN have reproduced the experimental curves with higher accuracy for metals with filled or nearly filled d bands, whereas HSE06 performs better for metals with more localized d states. The mechanical properties were considered in terms of Young's modulus; the outcomes revealed that metals which did not exhibit electronic d promotions possess higher values of the elastic modulus. This work highlights how electronic structure prediction, bond hybridization, and electronic promotion determine the properties of the considered metallic elements, highlighting the strengths and weaknesses of the three computational approaches and suggesting guidelines for obtaining reliable simulations for pure metal systems.

Introduction

Atomistic simulations are widely recognized as essential tools in materials science, offering a powerful means to investigate the intrinsic properties of metallic elements,[1] and organic,[2,3] and inorganic systems[4] at the atomic level. Modeling studies have been produced in recent years to investigate the boundary systems in terms of oscillations and turbulence, also considering thermal effects.[5,6] Using advanced computational techniques such as Density Functional Theory (DFT) and Molecular Dynamics (MD) simulations, it is possible to analyze the thermodynamic, mechanical, and structural behavior of many different systems across a range of conditions.[7–9] These methods enable the exploration of complex phenomena, including phase transformations, defect evolution, and mechanical responses that are often difficult to observe through experimental techniques.[10] In practical applications of DFT, the crucial aspect is the need corresponded to approximate the exchange–correlation (xc) functional; in fact, xc functionals can exhibit self-interaction and delocalization errors. One type of approach for these terms is local-density approximations (LDA), where the contribution of the corresponding homogeneous electron density system is equal to the local value of the density itself. This method is the simplest approximation, and it is local in the sense that the xc energy at any point in space is a function only of the electron density at that point.[11] Generalized gradient approximations (GGAs) are still local but also consider the density gradient in the same coordinates. Using the most recent GGAs, good results have been obtained for determining molecular geometries and ground-state energies.[12] Many further improvements have been made to DFT by developing better representations of the functionals. For example, hybrid functionals are a class of approximations to the xc energy that incorporate a portion of exact exchange (x) from Hartree–Fock theory with the rest of the xc energy from other sources, which could be *ab initio* or empirical.[13] Anyway, the most prominent strategy to improve the reliability of DFT has been the addition to the GGA approach of new corrective terms, leading to improved or broader accuracy.[14] Some historical examples of this have been the introduction of density gradients, Hartree–Fock exchange, kinetic energy density, various ways to include nonlocal correlation, and range separation.[15]

Focusing on metallic properties, the reliability and accuracy of atomistic simulations have been significantly improved through the choice of the best functional and the concomitant development of sophisticated interatomic potentials, including the Embedded Atom Model (EAM)[16] and the introduction of pseudopotentials (PPs).[17] The EAM is a semi-empirical method

[a]Department of Science and Engineering of Matter, Environment and Urban Planning, Polytechnic University of Marche, Ancona, Italy. E-mail: e.laudadio@staff.univpm.it
[b]Department of Information Engineering, Polytechnic University of Marche, Ancona, Italy

that describes interatomic interactions in metals, while PPs simplify the interaction between electrons and nuclei in quantum mechanical calculations. This aspect appears crucial for metals, since they can have many different core electron levels in their shell, and then the description of the electrons–nuclei interactions cannot be ignored.[18] This approach has shown success in describing properties of body centered cubic (bcc) metals such as tantalum, capturing key characteristics from elastic constants to dislocation behavior. Furthermore, the incorporation of atomistic techniques within multiscale modeling frameworks allows for a more holistic understanding of materials performance, bridging the gap between atomic interactions and macroscopic properties.[19]

Nonetheless, significant challenges continue to hinder the full potential of atomistic simulations in predictions of metal systems.[20,21] One major limitation is to accurately represent the complex grain boundary structures and their interactions with lattice defects, and these features are vital to the mechanical integrity and optical properties of metals. Additionally, the high computational demand required to simulate large-scale systems or long-time durations often forces compromises in model fidelity. Another persistent issue is the limited transferability of interatomic potential, as those calibrated for specific systems may perform poorly when applied to different environments or material states. Another important aspect to consider is that the quantum mechanical simulations have approximations to the Schrodinger equation, and the use of these terms is extremely specific for the metal type used. This means that a quantum mechanical method calibrated on a metal can be a worse choice to simulate another metal system.

In this paper, different quantum and classical mechanical atomistic approaches were used to simulate the electronic, optical, and mechanical properties of chromium, molybdenum, tungsten, nickel, palladium, platinum, copper, silver, and gold. These transition metals comprise groups 4B, 8B, and 9B of the periodic table, filling 4, 5, and 6 energy levels depending on the period to which they belonged. Cr, Mo, and W, in the 4B group, are known to adopt a bcc phase with the space group 229, while the 8B and 9B metals have a face-centered-cubic (fcc) phase, with the space group 225 (Table 1).

Each of these transition metals possesses unique physical properties that determine their industrial and technological applications. They are characterized by high electrical conductivity due to their metallic bonding and the presence of mobile valence electrons. For example, Ag has a high electrical conductivity of 63×10^6 S m^{-1}, applicable in high frequency electronic applications, followed by Cu and Au.[22] On the other hand, Mo and W are used in electronics (like OLED backplanes) because they maintain electrical performance and dimensional stability under extreme thermal stress.[23] Au and Pt are preferred for high-precision connectors and sensors because they do not oxidize, ensuring consistent contact resistance over time.[24] Moreover, Cr has a significantly higher electrical resistivity of 125 nΩ m at 20 °C and is used in high-performance electronics, industrial heating, and aerospace applications.[25] Measurement of optical constants like the refractive index and extinction coefficient for Ni shows consistent emissivity values at temperatures around their melting points.[26] This feature of Ni is critical for precise, non-contact temperature sensing in high-temperature metallurgy and aerospace engineering, ensuring that thermal modeling and radiation-based controls remain accurate during phase changes.[27] While alloys like Ni–Cr–Mo are engineered for high yield strength over 500 MPa and are used in demanding applications such as medical implants,[28] W and Mo are refractory metals with exceptionally high melting points and high creep resistance, allowing them to retain strength at temperatures where other metals soften.[29]

As mentioned above, these metals were chosen because they are currently used as components of many different devices, but despite this aspect, some of their properties are not always investigated in detail. This is due to the electron configuration of these metals, which is difficult to describe, since each of them shows external electronic configurations in which an n^s valence electron could be (or not) promoted to the $n - 1^d$ orbitals, completely or half-filling the energy shell. This means that the description of the energy of the free electrons of these materials is crucial to predict the behaviors of metals and for the hybridization phenomena. Furthermore, the literature in this respect is often contradictory, and in many cases, calculation methods that are presented as excellent show questionable reliability even in certain metallic contexts. For instance, Werner *et al.*[30] used DFT simulations to investigate the optical real and imaginary parts of the complex dielectric constant as well as the energy loss function (ELF) for some of these metals like Co, Ni, Cu, Mo, Pd, Ag, W, Pt, and Au. They found that the consistency between the DFT and the experimental data is better than 5% for all considered elements over the entire energy range considered; however, the atomistic calculations showed significant differences with the earlier optical data.

In this study, the electronic properties of the band structure and the density of states (DOS) calculations were reported for each metal. Then, optical properties in terms of the refractive index (n) and extinction coefficient (k) were considered with mentions about the interactions with the applied field and dispersive phenomena. To perform these calculations, three different quantum-mechanical methods were used for each metal. In detail, the GGA of the Perdew–Burke–Ernzerhof (PBE) functional[31] was used as the first method, then, the meta-GGA (MGGA) approach in terms of the R^{2}SCAN functional[32] was applied to determine the effect of the inclusion of local kinetic energy density of the electrons. Finally, the hybrid functional

Table 1 Structural properties of metals analyzed

Metal	Phase	Space group	Unit cell
Cr	bcc	229	2.885 Å^3
Mo	bcc	229	3.147 Å^3
W	bcc	229	3.165 Å^3
Ni	fcc	225	3.252 Å^3
Pd	fcc	225	3.890 Å^3
Pt	fcc	225	3.924 Å^3
Cu	fcc	225	3.615 Å^3
Ag	fcc	225	4.089 Å^3
Au	fcc	225	4.078 Å^3

Heyd–Scuseria–Ernzerhof (HSE06)[33] was utilized to investigate the effect of the inclusion of the exact Hartree–Fock (HF) exchange energy on the simulations. PBE provides a robust reference for itinerant metallic bonding, R^{2}SCAN offers a better balanced semilocal description of structural and energetic properties in transition metals, and HSE06 tests the sensitivity of the results to short-range exact exchange and d electron localization. The choice of these three different functionals concerns the need to identify the capabilities and limitations of each method for each simulated metal. The idea is to tailor the best prediction approach to use for each specific metal, choosing between these three different methods on the basis of the specific property to be predicted. Furthermore, mechanical properties in terms of Young's modulus were evaluated using a force field approach through molecular dynamics (MD) simulations. This means that different metals were investigated with different methodologies, underlining the ongoing challenges that must be addressed to enhance predictive accuracy in relation to the metal type. This approach is necessary to identify the best metal configuration to use for the fabrication of diodes, in order to maximize the performance of the device itself before even producing it.

Materials and methods

Quantum-mechanics methods

All the DFT-based simulations were carried out using the Quantum Atomistic ToolKit (Q-ATK).[34] Three different quantum mechanics methodologies were used for each metal. In detail, GGA-PBE, MGGA-R^{2}SCAN, and hybrid-HSE06 functionals were compared between them. The first method is based on the assumption that the exchange and the correlation energy at a point depends not only on the density at that point, but also on its gradient of electron density following eqn (i):

$$E_{xc}^{GGA}[n] = \int n(r)\in_{xc}(n(r), |\nabla n(r)|)\mathrm{d}r \quad \text{(i)}$$

in which the term $|\nabla n(r)|$ is the addition for the gradient, and the density $n(r)$ represents the number of electrons per unit volume. In the second method, an additional term is included following eqn (ii):

$$E_{xc}^{MGGA}[n] = \int n(r)\in_{xc}(n(r), |\nabla n(r)|, \tau(r))\mathrm{d}r \quad \text{(ii)}$$

where the kinetic energy density is defined as the following summation over all occupied orbitals (r) following eqn (iii)

$$\tau(r) = \frac{1}{2}\sum_{i}^{occ}(\nabla\varphi_i(r))^2 \quad \text{(iii)}$$

The hybrid HSE06 functional involves a screened exchange–correlation energy that mixes the short-range exact Hartree–Fock exchange with the PBE exchange and correlation energy. This means that the PBE functional is used for the long-range part, and it includes a specific screening parameter (m = 0.2 Å^{-1}). The general formula can be expressed as eqn (iv)

$$E_{xc}^{HSE06} = \tfrac{1}{4}E_x^{HF,sr}(m) + \tfrac{3}{4}E_x^{PBE,sr}(m) + E_x^{PBE,lr}(m) + E_c^{PBE} \quad \text{(iv)}$$

where $E_x^{HF,sr}(m)$ is the Hartree–Fock (exact) exchange component, which is limited to the short-range (sr) part of the Coulomb potential and screened by a parameter m; $E_x^{PBE,sr}(m)$ is the PBE exchange energy component for the short-range part, also screened by m; $E_x^{PBE,lr}(m)$ is the PBE exchange energy component for the long-range (lr) part of the potential, which is not screened; E_c^{PBE} is the standard PBE correlation energy functional. This approach uses a mixing parameter of 25% for the exact exchange (1/4) and a screening parameter m of 0.2 Å^{-1}.

For each simulation, despite the functional, each approximation was coupled with LCAO Ultra description of Basis set and Norm-conserving PseudoDojo PPs.

This means that for this formalism, the single-electron eigenfunctions, ψ_α, are expanded in a set of finite-range atomic-like basis functions φ_i following eqn (v):

$$\psi_\alpha(r) = \sum_i c_{\alpha i}\varphi_i(r) \quad \text{(v)}$$

An energy cut-off was set to 150 hartree with a k-point density sampling of 20 Å^3. The DOSs were calculated considering an energy range of 10 eV above and 10 eV below the Fermi level. In the optical spectra, 20 bands above and 20 bands below the Fermi level were considered, with an energy range between 1 and 4 eV, and writing 801 points per graph with a k-point density of 28 Å^3. For each metal, intraband contributions were also considered together with the plasma frequency and the inverse lifetime as follows:

Plasma frequency: 11 eV (Cr), 3 eV (Mo), 10.99 eV (W), 4.88 eV (Ni), 7.4 eV (Pd), 5.145 eV (Pt), 8.76 eV (Cu), 9.013 eV (Ag), 8.9 eV (Au).

Inverse lifetime: 4.68 × 10^{14} Hz (Cr), 1 × 10^{14} Hz (Mo), 1 × 10^{15} Hz (W), 1 × 10^{14} Hz (Ni), 1 × 10^{14} Hz (Pd), 1.67 × 10^{15} Hz (Pt), 8.34 × 10^{14} Hz (Cu), 4.35 × 10^{12} Hz (Ag), 4.35 × 10^{12} Hz (Au).

The choices of k-point density sampling, cut-off energy, and convergence criteria were retained moving between different functionals to avoid variables in the comparison.

Classical-mechanics methods

For each metal, a simulation box of x = 10 nm, y = 10 nm, z = 100 nm was generated, including periodic boundary conditions (PBCs) along the x and y axes. After a minimization step, an equilibration phase was adopted to introduce the room temperature effect for generating the velocity of motions. Then, a production phase of 100 ns was performed. GROMACS 2023.3 software[35] was chosen for MD simulations. The CHARMM27 force field was adapted for metals by modifying the Lennard-Jones parameters for metal–metal interactions.[36] Young's in-plane modulus was calculated using the deformation dashboard in the .mdp file, applying stress and strain in the simulation box along the z-direction. Then, the Vir-ZZ and P-ZZ terms were detected as stress using the gmx energy gromacs tool and the displacement of metal systems rather than the initial length was determined as strain. The stress–strain curve was finally

obtained for each metal, and the slope of the initial region was the Young's in-plane modulus value.

From a theoretical point of view, Young's in-plane modulus was obtained using eqn (vi).

$$Y_s = \frac{1}{A_0}\frac{\partial^2 E_s}{\partial \varepsilon^2} \quad \text{(vi)}$$

where A_0 is the cross-sectional area of the unit cell at the equilibrium position and E_s is the strain energy whose second derivative is computed with respect to the strain ε. To calculate $\partial^2 E_s/\partial\varepsilon^2$, the compressive and tensile strains were identified as negative and positive percentages, respectively. At the first step, the relaxed unit cell of each metal was subjected to uniaxial compressive and tensile loading, changing the pressure applied to the simulation box. Using this approach, $\partial^2 E_s/\partial\varepsilon^2$ was calculated and then substituted in the equation to obtain the in-plane Young's modulus.

Results

Electronic properties

Analyzing the DOS obtained for Cr reveals that the peaks obtained with PBE and R^{2}SCAN are very similar *i.e.*, the conduction and valence band profiles show slight shifts towards the Fermi level. The curves obtained with HSE06, indeed, indicated the evident shift of the valence band from the Fermi level and lower density of the conduction bands. This is attributable to the fact that the exact Hartree–Fock contribution allows for a more detailed description of the excited states. The graphs for Mo follow the same trend previously described, with a clear agreement between the results obtained with PBE and R^{2}SCAN. In this case, despite a more evident shift in the peaks, which move away from the Fermi level, the description obtained with HSE06 also seems to follow the trend highlighted with the other two functionals (Fig. 1). This type of result is also observed in W; in fact, the signals are evidently the same, with a greater shift when using the hybrid functional. This means that the functionals are in greater agreement with each other in simulating the DOS of Mo and W, and even if there is a more evident discrepancy for Mo, these results demonstrate how, surprisingly, the energy level influences the prediction. Indeed, valence electrons in shells closer to the nucleus seem to suggest a more marked difference in description, which attenuates as the valence level increases.

Inspection of the data calculated from DOS for Ni, Pd, and Pt shows that a common trend is observed. In fact, in every case, the results obtained with PBE and R^{2}SCAN are superimposable, therefore, it is not possible to notice whether the contribution of the local kinetic energy density of the electrons is present. The outcomes predicted with the hybrid functional are characterized by an underestimation in terms of signal intensity, but with the same position of the signals in the conduction band; conversely, a clear shift of the peaks in the conduction band is observed (Fig. 2). These results show how, in this case the functionals exhibit different degrees of accuracy as the simulated energy in the DOS increases. For the values below and close to the Fermi level, the simulations are in excellent agreement with each other, while above 6 eV, marked differences are observed, especially using HSE06.

Finally, evaluating the DOS calculations of the metals Cu, Ag, and Au indicated that a common trend is also evident with the peaks approximated with PBE and R^{2}SCAN, which are very similar, particularly for Cu, although not overlapping as in the previous case. Also in this group, the results obtained with HSE06 differ from those gained with the other two systems. For H in this case, the shift away from the Fermi level is much more evident than for the metals in the different groups, although the intensity of the peaks in terms of eV^{-1} is in line with the other results (Fig. 3). In this case, the determining factor appears to be the large number of valence electrons, whose approximations in any case determine more marked differences, regardless of the energy level.

To summarize, the DOS investigation highlighted that for metals with partial filling of the d orbitals (*i.e.*, Cr, Mo, and W), the methods exhibit different sensitivities, with greater discrepancies being found at lower energy levels. The simulations of group 8B metals show the best agreement among them, with no effects of energy shells or electronic promotions, which is surprising. Finally, the analysis of the metals Cu, Ag, and Au highlighted an increased discrepancy between the methods beyond the simulated 6 eV, demonstrating a reliability that depends on the simulated field range. The shifts detected with the use of HSE06 were quantified using the Fermi level as a reference. In terms of agreement with the experimental data, these shifts are a bit far from the experimental values, thus

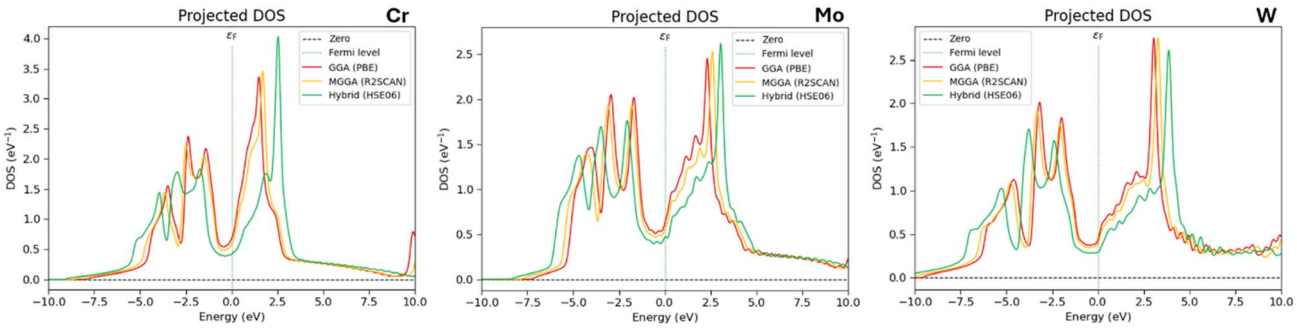

Fig. 1 Comparison of the DOS of chromium (left), molybdenum (center), and tungsten (right). Data obtained with PBE (in red), R^{2}SCAN (in yellow), and HSE06 (in green) functionals are compared.

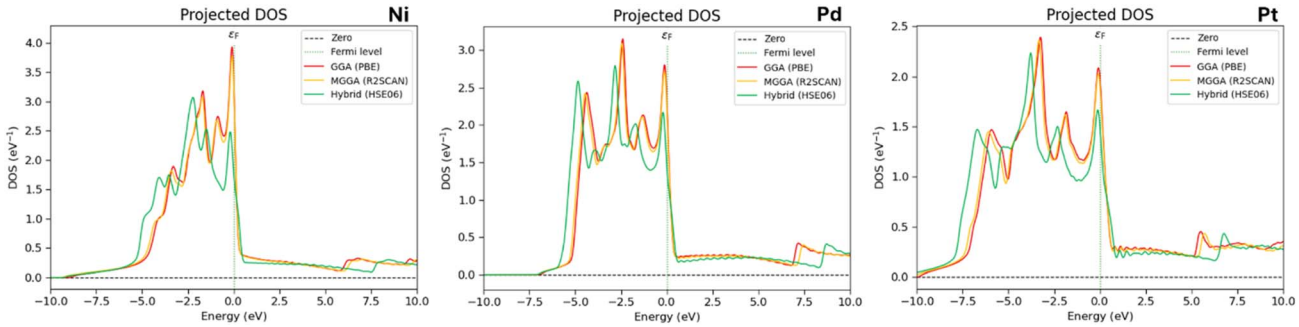

Fig. 2 Comparison of the DOS of nickel (left), palladium (center), and platinum (right). Data obtained with PBE (in red), R^{2}SCAN (in yellow), and HSE06 (in green) functionals are compared.

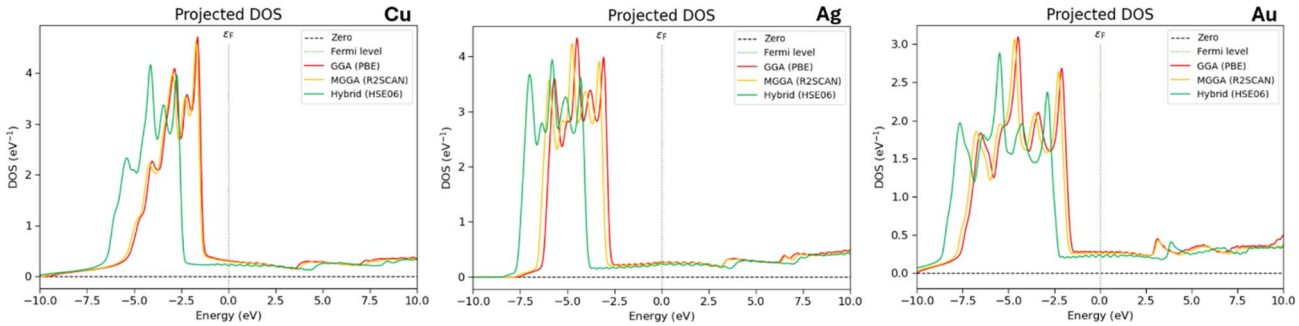

Fig. 3 Comparison of the DOS of copper (left), silver (center), and gold (right). Data obtained with PBE (in red), R^{2}SCAN (in yellow), and HSE06 (in green) functionals are compared.

determining PBE and R^{2}SCAN as more suitable for this type of calculation for metals. The reason for this discrepancy could be ascribed to the treatment of delocalized itinerant d electrons in HSE06, in which this effect is delicate. Indeed, the metallic systems screen exchange strongly; thus, the physically appropriate exact-exchange fraction is smaller, and HSE06 can overshift the d manifold, also overestimating magnetic splitting.

Another reason for the discrepancy in the use of HSE06 is surely attributable to the inclusion of exact Hartree–Fock exchange, affecting the electronic structure of delocalized and localized d-electron systems. In more detail, this makes the localized d electron states less spuriously delocalized, increasing the separation between occupied and empty d levels, and strengthening the exchange splitting enough to open or enlarge d-derived gaps. About the delocalized itinerant d electrons, the metallic systems screen the exchange contribution strongly; thus, the physically appropriate exact-exchange fraction is smaller, and HSE06 can over-shift the d manifold, also overestimating magnetic splitting. This means that the effect is more delicate for delocalized d electrons, and HSE06 appears more beneficial for localized d electrons.

Optical properties

The optical properties of the different metals were investigated through the simulation of n and k obtained using three different functionals previously described. The calculation values were then compared to the experimental values found in the literature in the energy range from 1 to 4 eV. We chose this energy range following the availability of the experimental data for comparison. The discrepancy in terms of absolute values of optical properties in the energy range detected was used as a quantification criterion for the accuracy. The different metals studied were then divided based on their respective groups on the periodic table.

Fig. 4 shows the results approximated for the 4B group metals (Cr, Mo, and W). For Cr, all the computational methods used yield similar values for n. Among them, the hybrid functional HSE06 provides values which are closer to the experimental results,[37] particularly within the 1.3–2.3 eV energy range, and this is correlated with the additional term of the exact Hartree–Fock exchange contribution included in HSE06. On the other hand, at higher energies, an increased discrepancy was observed, and all computational methods systematically gave overestimated values, meaning that the inclusion of the exact exchange contribution is not enough to mimic the Cr behavior at high energies. With regard to the k, a significant deviation from the experimental curves was detected, with all the methods that tend to overestimate the experimental values.[37] The results for Mo reveal high degrees of consistency across all computational methods. In fact, the n was slightly overestimated with respect to the experimental data, and while starting from approximately 2 eV, the calculated values correctly approximated the experimental results.[38] For W, all the computational methods give similar results. The R^{2}SCAN functional approximated almost perfectly the experimental n

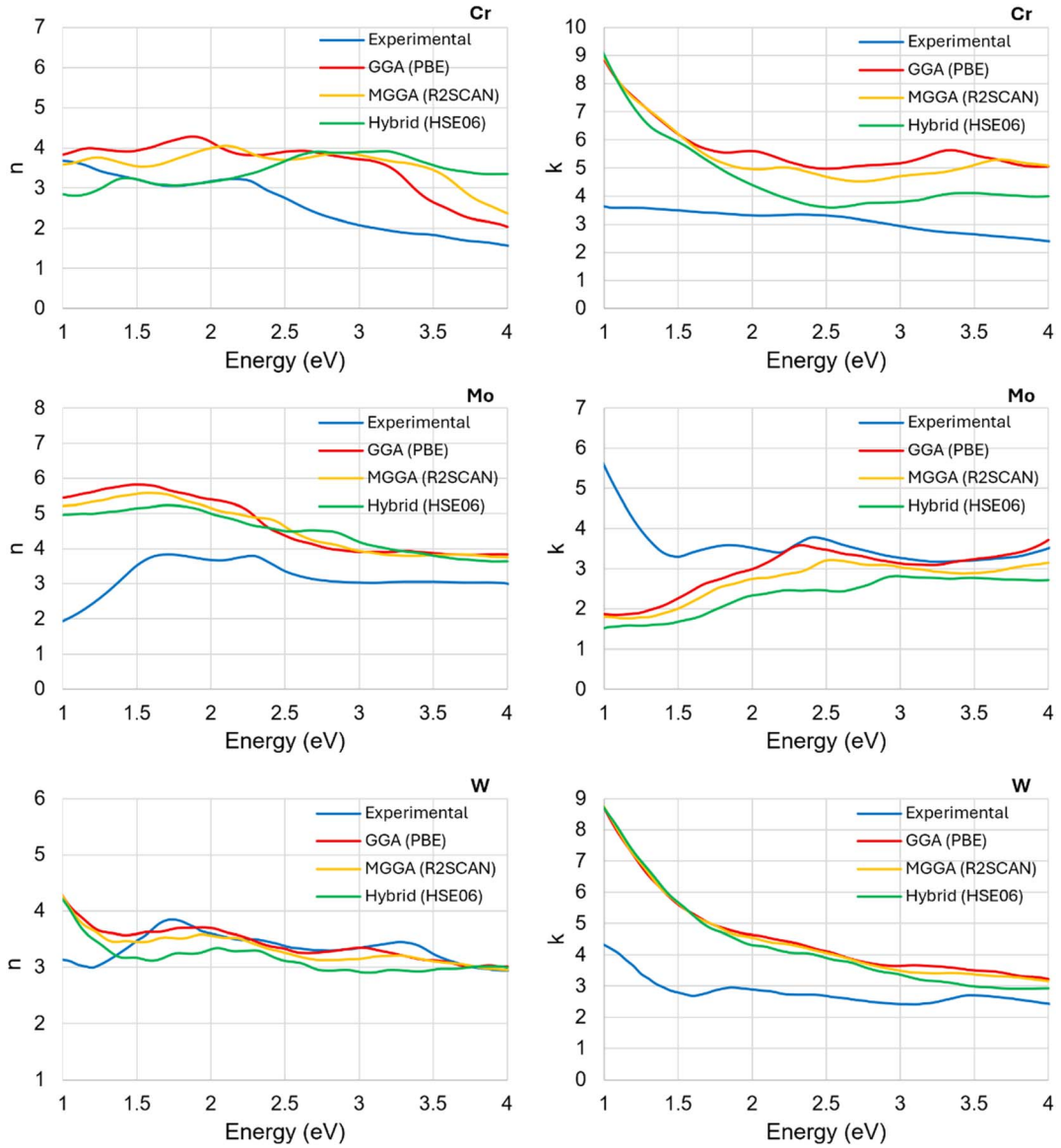

Fig. 4 Comparison of the refractive index (left) and extinction coefficient (right) of chromium (on the top), molybdenum (in the middle), and tungsten (at the bottom). Data obtained with PBE (in red), R^{2}SCAN (in yellow), and HSE06 (in green) functionals are compared to the experimental values (in blue) found in the literature.

from about 1.4 eV, while all the methods tended to overestimate the k compared to the experimental values,[38] particularly in the low-energy range, up to approximately 3 eV. This means that to better replicate the k, the MGGA approach in the use of R^{2}SCAN seemed to work a bit better than the other methods. The local kinetic energy density of the electrons is a necessary parameter to consider, which is the most important part of the MGGA R^{2}SCAN method.

Fig. 5 shows the comparison between computational and experimental n and k for metals of the group 8B (Ni, Pd, and Pt). For Ni, both these optical properties were well described by all the computational methods. The PBE and R^{2}SCAN functionals provided almost identical results, which appeared well aligned with the experimental curves for both n and k.[38] In the low-energy range, the n values from PBE and R^{2}SCAN tended to be overestimated, and this overestimation is more evident using the HSE06 functional with respect to the experimental curve. The analysis of Pd reveals that the experimental n was better reproduced by R^{2}SCAN/PBE functionals, while all methods provided an almost perfect approximation of the experimental curves of the k.[37] The results for Pt (Fig. 5, on the bottom) show that all the functionals used are able to approximate the experimental values well.[38] The best outcomes were obtained with R^{2}SCAN/PBE functionals, while HSE06 tended to slightly overestimate the data. However, at lower energies, the results fit the experimental curve worse. For the k, all methods gave good results. Although the curve obtained with HSE06 better represents the shape of the experimental one, the values obtained using R^{2}SCAN/PBE functionals were in better agreement with the data.[38] This means that the trend for the metals in group 8B

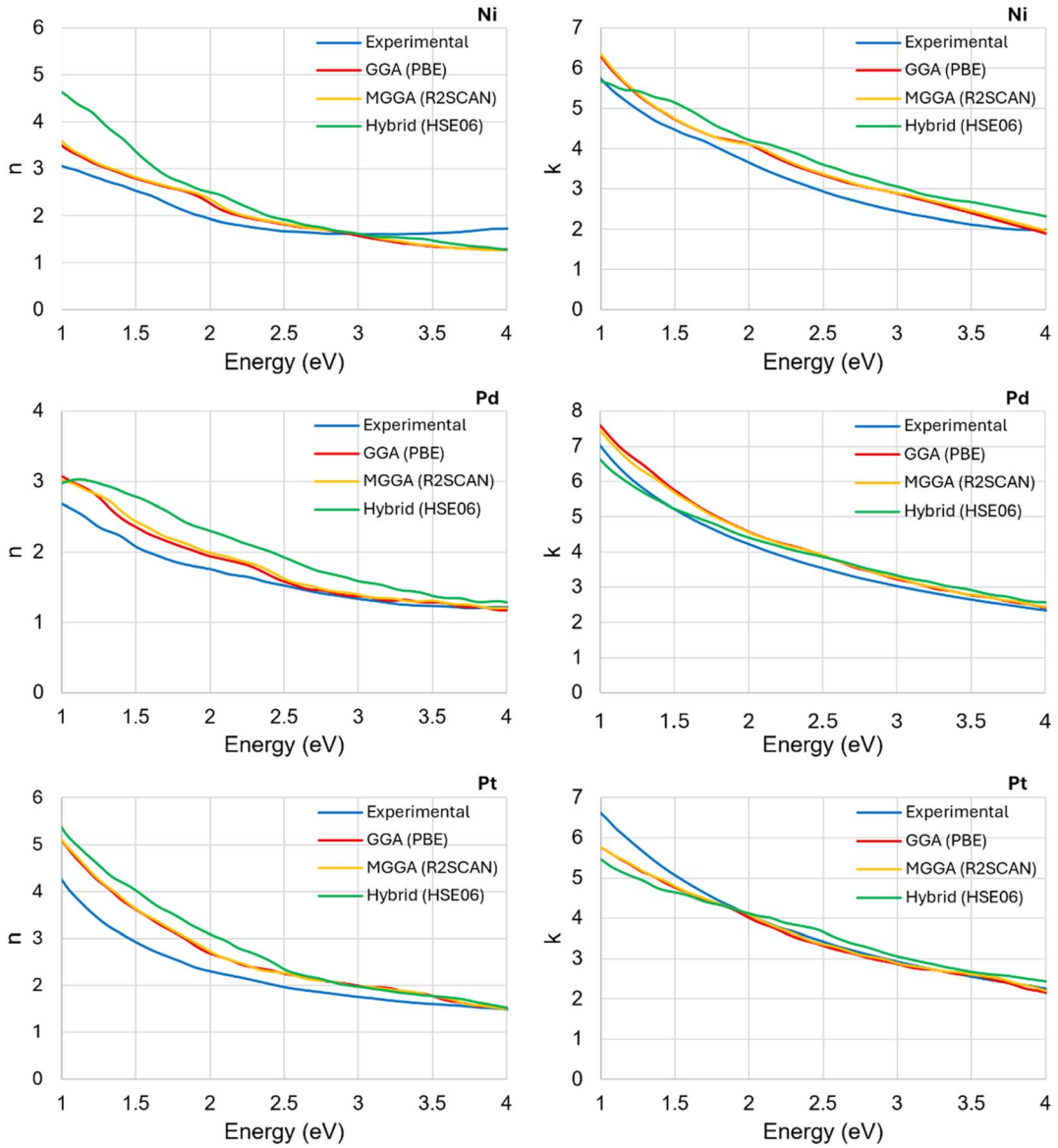

Fig. 5 Comparison of the n (left) and k (right) of nickel (on the top), palladium (in the middle), and platinum (at the bottom). Data obtained with PBE (in red), R^{2}SCAN (in yellow), and HSE06 (in green) functionals are compared to the experimental values (in blue) found in the literature.

seems to be inverted with respect to that observed in group 4B, suggesting that the GGA and MGGA approaches could be more accurate with the increase in the number of valence d electrons.

Fig. 6 shows the comparison of the n and k for metals of the group 9B (Cu, Ag, and Au). For Cu, the n calculated with PBE and R^{2}SCAN is slightly overestimated and shifted to the left when compared to the experimental curve.[38] The values of the n obtained with HSE06 were better consistent with the experimental data, while for the k, HSE06 yielded underestimated values,[39] and the best results were provided by PBE/R^{2}SCAN. For Ag, the HSE06 functional provided results in perfect accordance with the experimental values for both the n and the k,[38,39] while the PBE and the R^{2}SCAN functionals indicate slightly overestimated/underestimated values for the n/k, particularly at higher energies. Moreover, both the simulated curves of n and k were left shifted with respect to the experimental ones. The n of Au was correctly described by the HSE06 functional, while other methods showed a greater deviation from experimental values.[38] However, for the k, from approximately 2.5 eV, HSE06 underestimated the experimental data,[39] while PBE and R^{2}SCAN functionals appeared to be a better choice in this energy range.

In summary, PBE and R^{2}SCAN functionals generally yielded similar results, while the HSE06 functional almost always showed a deviation. Furthermore, the functionals had different reliability not only depending on the metal and the type of hybridization, but also in relation to the applied field strength. In fact, in many cases, the results showed variable accuracy depending on the field strength, thus outlining reliabilities that were not always equal.

To summarize, PBE and R^{2}SCAN give more precise results for metals with filled or nearly filled d bands, while HSE06 excels for more localized d states. To provide a physical explanation,

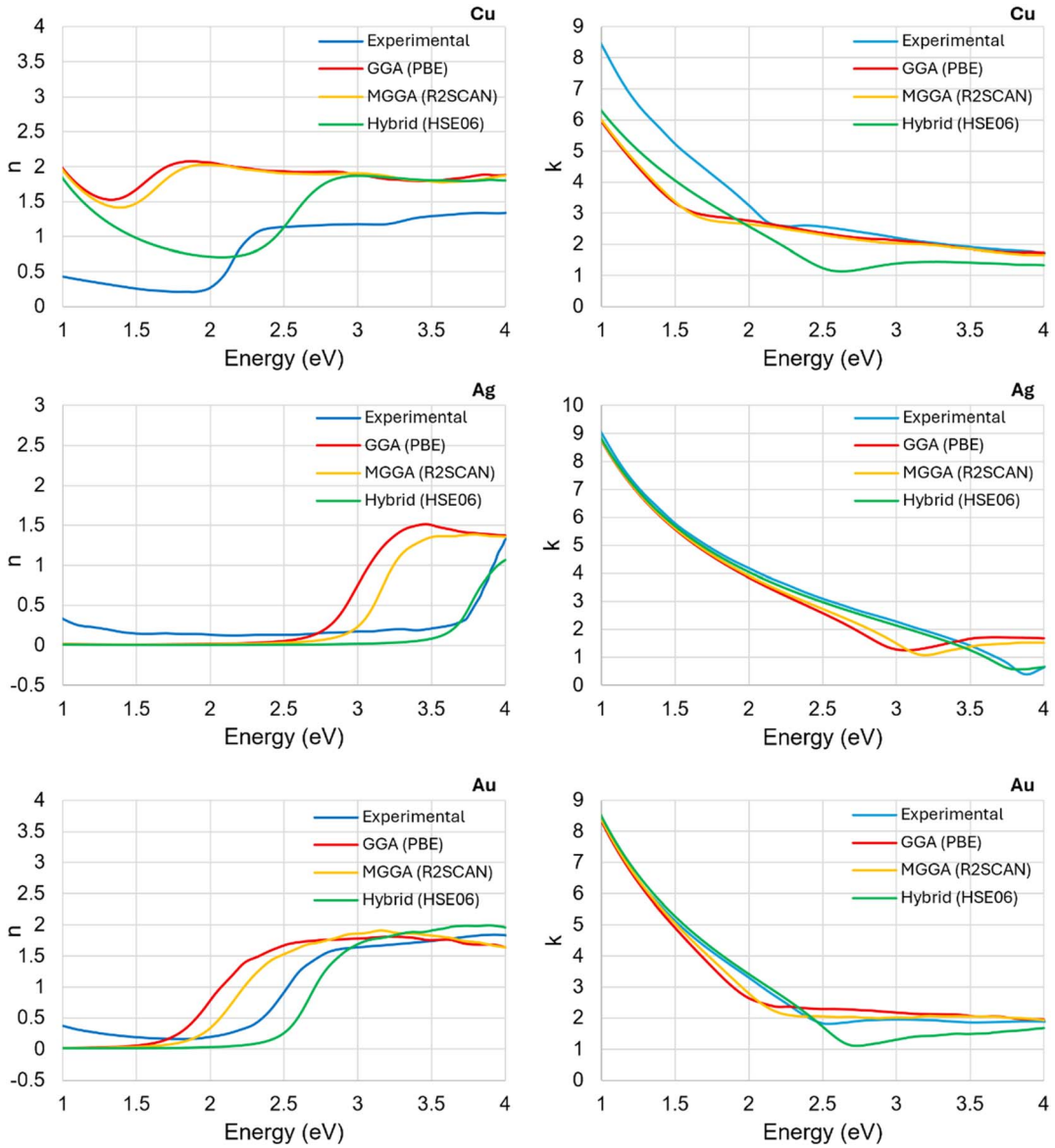

Fig. 6 Comparison of the *n* (left) and *k* (right) of copper (on the top), silver (in the middle), and gold (at the bottom). Data obtained with PBE (in red), R^{2}SCAN (in yellow), and HSE06 (in green) functionals are compared to the experimental values (in blue) found in the literature.

the key issue is screening *versus* localization. As the d manifold becomes more filled and more metallic, the electrons become more itinerant and the system screens exchange more efficiently. In that limit, the physically appropriate amount of exact exchange becomes very small. PBE and R^{2}SCAN perform better for metals with filled or nearly filled d bands: both remain semilocal, so they preserve the short-ranged, strongly screened exchange–correlation picture that is appropriate for itinerant metallic bonding. In bulk-solid benchmarks, PBE is quite good for metals, while R^{2}SCAN results are especially well balanced for cell volumes, cohesive energies, and related properties across 3^d, 4^d, and 5^d transition metals. By contrast, for more localized d states, the main problem of semilocal functionals is self-interaction or delocalization error: they tend to spread the d electrons too much and underestimate the separation between occupied and empty d levels. HSE06 helps precisely this point, because its screened Hartree–Fock exchange removes part of that error and stabilizes a more atomic-like picture of localized d-electrons.

To conclude, itinerant, strongly screened d-band metals favor PBE and R^{2}SCAN; narrow-band, weakly screened, localized d states favor HSE06. The same mechanism that helps HSE06 for localized electrons can actually make it too aggressive for true metals, where screened hybrids have even been shown to spuriously stabilize ferromagnetism and not systematically improve transition-metal surface chemistry over PBE.

Mechanical properties

The mechanical properties were then calculated in terms of the Young's modulus of each metal investigated. Hardness is the property of solid materials expressing resistance against permanent or plastic deformation. Different responses to pressure

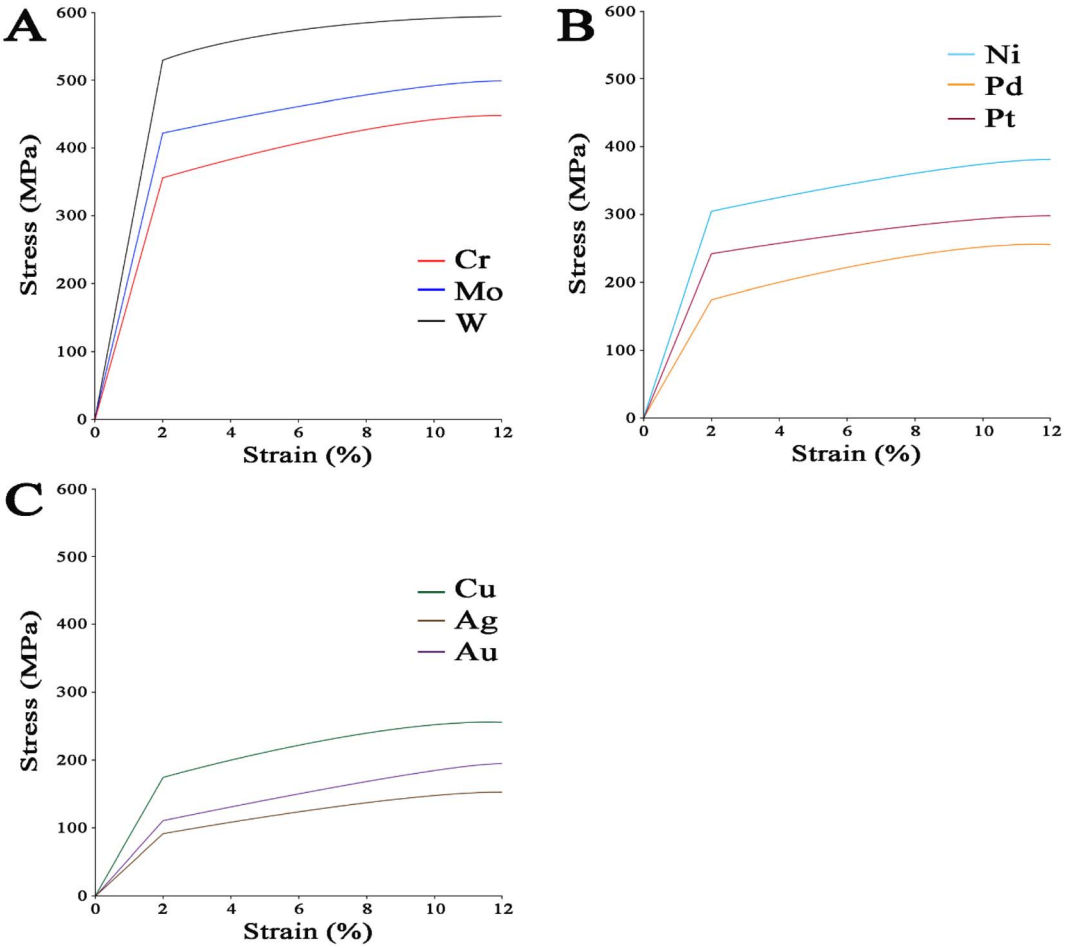

Fig. 7 Stress–strain ratio for the metals of 4B (A), 8B (B), and 9B (C) groups.

variation along the z direction were registered for each metal (Fig. 7). The dependence of Young's modulus on composition is non-systematic; on the other hand, the metal type considered has some peculiar effects. In general, Young's modulus tends to increase with increasing connectivity,[40] but in this case, since transition metals are investigated, the hybridization phenomena occurring in the metal atoms are crucial to identify the elastic response of metals. From our results, Cr, Mo, and W, which exhibit the bcc phase, have higher Young moduli with respect to those of the other metals, which adopt the fcc phase. Bcc and fcc structures in metals exhibit different mechanical properties due to their differing atomic arrangements and slip systems. The bcc structures resulted in stronger and harder materials, and on the other hand, less ductile materials. The fcc structures are more ductile, thus possessing higher toughness. This difference in mechanical behavior is influenced by the number of slip systems, the ease of dislocation motion, and the packing density of atoms within each structure. Comparing the three bcc phase systems among them, W showed the highest Young modulus, reaching 360 GPa, while Mo had a value of 315 GPa. Cr has the highest value below 300 GPa, with a value of 252 GPa. This trend is in line with the literature, which indicates that Young's modulus increases from top to bottom along the group in the periodic table (*i.e.*, increasing period number). Cr promotes an electron from 4^s to 3^d orbitals to partially fill all five 3^d orbitals. Mo shows the same behavior, with the promotion of an electron from 5^s to 4^d orbitals, which is more favored with respect to Cr. On the other hand, W does not seem to behave in the same way. The reason is ascribed to the higher number of protons in W nuclei, which exert a stronger attraction to the electrons that will move closer to the nucleus. The 6^s electrons will remain more in the shielding core, so they aren't shielded as much as the 5^d electrons, leading to the inert pair effect. The difference in energy between the 6^s and 5^d orbitals, which is higher than between the 5^s and 4^d orbitals, is larger than the energy gained from the exchange energy by promoting the ns electron to the $n - 1^d$ orbital, as shown by Cr and Mo. Electron promotion seems to influence the strength of bonding, decreasing the Young's modulus of metals.

On analyzing the slope obtained for the fcc metals, the expected trend of Young's modulus is respected along the same period in the periodic table, since it increases from right to left. Ni exhibited the highest Young's modulus observed for fcc systems, reaching 204 GPa, and no electron promotion was observed, confirming the previously reported notion about the influence on the strength of bonds regardless of the lengths. On the other hand, Pd shows an important decrease in Young modulus, reaching 119 GPa. This value is in line with the literature, and to explain this trend, it's important to note that

Table 2 Elastic properties of metals in relation to the face

Metal type	Young's modulus (exp)	Young's modulus (sim)	Face	Bond length
Cr	240–260 GPa (ref. 41)	252 GPa	bcc	2.50 Å
Mo	310–330 GPa (ref. 42)	315 GPa	bcc	2.73 Å
W	340–405 GPa (ref. 43)	360 GPa	bcc	2.74 Å
Ni	190–220 GPa (ref. 44)	204 GPa	fcc	2.49 Å
Pd	115–125 GPa (ref. 45)	119 GPa	fcc	2.75 Å
Pt	154–172 GPa (ref. 46)	165 GPa	fcc	2.77 Å
Cu	110–130 GPa (ref. 47)	120 GPa	fcc	2.56 Å
Ag	69–74 GPa (ref. 48)	72 GPa	fcc	2.89 Å
Au	76–81 GPa (ref. 49)	80 GPa	fcc	2.88 Å

Pd promotes both $5s^2$ electrons to completely fill the 4d orbitals. Pt exhibits a modulus of 165 GPa, it has a partially filled 5^d orbital, and the 6^s orbital can be involved in bonding, making it more susceptible to electron promotion. To analyze the behavior of metals in the 8B group, the double promotion in Pd leads to the smallest Young's modulus, Pt shows an intermediate value, with promotion of one electron, and finally, Ni shows the highest value, and it does not promote electrons.

Cu has a Young's modulus of 120 GPa, with the promotion of 4^s to 3^d orbitals to completely fill them, while Ag showed the lowest Young's modulus with a value of 72 GPa, again promoting an $n + 1^s$ electron to the n^d level.

Finally, Au has an intermediate value of 80 GPa, completing the 5^d orbitals with the promotion of one 6^s electron. To conclude, the two main effects on the elastic properties of metals investigated are the phase, since the bcc structure exhibited high hardness, and the electron promotion, which decreases the strength of chemical bonds. Moreover, it is interesting to note that no correlation between the Young's modulus and bond length was observed, to show the importance of identifying short-range phenomena in terms of electron propagations (Table 2).

To summarize the analysis of elastic moduli, even if the metals with bcc have higher Young's moduli compared to those with fcc, the crystal symmetry is not always specific for a trend in elastic moduli. On the other hand, the most critical aspect to determine Young's modulus is related to the bonding hybridization, and the metals which do not exhibit electronic promotion preserve higher values.

Conclusions

In the present study, nine metals from three different groups of the periodic table such as 4B (Cr, Mo, and W), 8B (Ni, Pd, and Pt), and 9B (Cu, Ag, and Au), were investigated in terms of electronic, optical, and mechanical properties using three different functionals of PBE, R^2SCAN and HSE06. The results related to the electronic properties reveal that the PBE and R^2SCAN functionals predicted similar results in terms of DOS profiles, confirming that the inclusion of the kinetic energy density term in R^2SCAN does not significantly alter the description of metallic elements. In contrast, the hybrid functional HSE06 led to energy shifts, reflecting its improved treatment of exchange interactions.

In more detail, the DOS calculations of different metals show that the elements with partial filling of the d orbitals like Cr, Mo, and W, are more sensitive to the functional used. Furthermore, the Ni, Pd, and Pt metals indicated a great agreement among them below the Fermi level, while the HSE06 functional approximated higher intensity of the DOS curves in all three cases. In addition, the analysis of the last group of the metals (Cu, Ag, and Au) highlighted a high discrepancy between the methods since increasing the number of valence electrons can remarkably affect the predictions with respect to the metals from 4B and 8B.

The optical spectral calculations indicated that for metals such as Ni, Pd, and Pt, PBE and R^2SCAN functionals are more consistent for metals with delocalized electrons, while HSE06 provides a better description and results closer to the experimental data for others (Cr or Ag).

Regarding the mechanical properties, the results confirmed that bcc metals (Cr, Mo, and W) exhibit higher Young's moduli than fcc metals (Ni, Pd, Pt, Cu, Ag, and Au), in agreement with experimental data.

These results provide guidelines in the choice of the correct computational method for each type of metal, with the aim to design the best diodes in terms of performance in the specific frequency range of work. Since many papers investigate materials with metals in complexes with other elements, such as O, S, Se, or Te, one of the novelties is the investigation of the advanced properties of these metals in pure state, because the literature to date is extremely lacking in this regard. Further theoretical investigation will focus on the key parameters for metals used in diodes such as evaluating the metal's work function, and evaluating their electrical resistivity and conductivity as well as thermal stability.

Conflicts of interest

There are no conflicts to declare.

Data availability

This study was carried out using publicly available data about the experimental curves of optical properties from: https://doi.org/10.1103/PhysRevB.9.5056 at https://journals.aps.org/prb/abstract/10.1103/PhysRevB.9.5056 (in which we used the experimental curves for Cr, Ni, and Pd), https://doi.org/10.1016/C2009-0-20920-2 at https://www.sciencedirect.com/book/edited-volume/9780080547213/handbook-of-optical-constants-of-solids (in which we used the experimental curves

for Mo, W, Pt, Cu, Ag, and Au). These experimental data were used to validate our simulation results. All data supporting the findings of the study are included within the article.

Acknowledgements

This work is part of the research of HORIZON-EIC-2023-PATHFINDERCHALLENGES-01-05 "Powering Satellites by a Combination of Solar and Microwave Energy Harvesting" (POWERSAT) (grant agreement no. 101162320).

References

1 J. A. Moriarty, J. F. Belak, R. E. Rudd, P. Söderlind, F. H. Streitz and L. H. Yang, *J. Phys.: Condens. Matter*, 2002, **14**, 2825.
2 A. Gavezzotti, L. Lo Presti and S. Rizzato, *CrystEngComm*, 2022, **24**, 922–930.
3 E. Laudadio, R. Galeazzi, G. Mobbili, C. Minnelli, A. Barbon, M. Bortolus and P. Stipa, *ACS Omega*, 2019, **4**, 5029–5037.
4 K. Kanhaiya, M. Nathanson, P. J. in't Veld, C. Zhu, I. Nikiforov, E. B. Tadmor, Y. K. Choi, W. Im, R. K. Mishra and H. Heinz, *J. Chem. Theory Comput.*, 2023, **19**, 8293–8322.
5 Z. Ullah, M. M. Alam, B. Ali, R. Rzig, H. Abu-Zinadah, M. Boujelbene and N. Ben Khedher, *Chaos, Solitons Fractals*, 2025, **198**, 116639.
6 M. Almheidat, Z. Ullah, M. A. Said, M. Hussien, S. Al Arni, M. D. Alsulami, A. O. Ibrahim and A. A. Faqihi, *Case Stud. Therm. Eng.*, 2024, **60**, 104812.
7 S. Zhao, Y. Osetsky and Y. Zhang, *Phys. Rev. Mater.*, 2019, **3**, 103602.
8 P. Huang, Q. Xiao, W. Hu, B. Huang and D. Yuan, *Metals*, 2024, **14**(4), DOI: 10.3390/met14040454.
9 B. Zhang, Y. Guo, Z. Liu, M. Li, D. Shi, Y. Li, J. Song, M. Bu and S. Du, *J. Alloys Compd.*, 2021, **857**, 157486.
10 V. Van Speybroeck, *Philos. Trans. R. Soc., A*, 2023, **381**, DOI: 10.1098/RSTA.2022.0239.
11 D. Bagayoko, *AIP Adv.*, 2014, **4**, 127104.
12 X. Shao, W. Mi and M. Pavanello, *J. Chem. Theory Comput.*, 2021, **17**, 3455–3461.
13 A. S. Nair, L. Foppa and M. Scheffler, *Sci. Data*, 2025, (12), 1–8.
14 R. Xia, R. N. Wu, Y. L. Liu and X. Y. Sun, *Materials*, 2015, **8**, 5060–5083.
15 D. E. Spearot, R. Dingreville and C. J. O'Brien, *Handbook of Mechanics of Materials*, 2019, pp. 357–390.
16 M. S. Daw and M. Chandross, *Acta Mater.*, 2023, **248**, 118771.
17 E. Mohebbi, E. Pavoni, L. Pierantoni, P. Stipa, E. Laudadio and D. Mencarelli, *J. Phys. Chem. Solids*, 2024, **185**, 111755.
18 I. B. Obot, K. Haruna and T. A. Saleh, *Arabian J. Sci. Eng.*, 2018, **44**, 1–32.
19 L. A. Zepeda-Ruiz, A. Stukowski, T. Oppelstrup, N. Bertin, N. R. Barton, R. Freitas and V. V. Bulatov, *arXiv*, 2020, preprint, arXiv:1909.02030, DOI: 10.48550/arXiv.1909.02030.
20 T. Hammerschmidt, J. Rogal, E. Bitzek and R. Drautz, *Nickel Base Single Crystals across Length Scales*, 2022, pp. 341–360.
21 L. Zhang, C. Lu and K. Tieu, *Comput. Mater. Sci.*, 2016, **118**, 180–191.
22 A. H. Alshehri, M. Jakubowska, A. Młozìniak, M. Horaczek, D. Rudka, C. Free and J. D. Carey, *ACS Appl. Mater. Interfaces*, 2012, **4**, 7007–7010.
23 J. Xiao, T. Li, V. M. Mastronardi, K. Kwak, H. Yoon, S. Hong and B. H. Kang, *Micromachines*, 2024, **15**, 1476.
24 Y. A. Abdelaziz, *Noble Met.*, 2012, DOI: 10.5772/33116.
25 K. Inoue, Y. Nakamura and N. Kunitomi, *J. Phys. Soc. Jpn.*, 2013, **27**, 1159–1164.
26 S. Krishnan and P. C. Nordine, *JAP*, 1996, **80**, 1735–1742.
27 G. Wang, K. Yu, Y. Bai, L. Li, K. Zhang and Y. Liu, *Energy*, 2024, **300**, 131651.
28 A. Haider, S. H. I. Jaffery, A. N. Khan, S. I. Butt and X. Jing, *J. Mater. Res. Technol.*, 2024, **30**, 7495–7509.
29 C. L. Briant and M. K. Banerjee, *Ref. Mod. Mater. Sci. Mater. Eng.*, 2016, DOI: 10.1016/b978-0-12-803581-8.02584-4.
30 W. S. M. Werner, K. Glantschnig and C. Ambrosch-Draxl, *J. Phys. Chem. Ref. Data*, 2009, **38**, 1013–1092.
31 S. Bhattacharjee, N. A. Koshi and S. C. Lee, *Phys. Chem. Chem. Phys.*, 2024, **26**, 26443–26452.
32 S. Swathilakshmi, R. Devi and G. Sai Gautam, *J. Chem. Theory Comput.*, 2023, **19**, 4202–4215.
33 R. Pawar and A. A. Sangolkar, *Comput. Theor. Chem.*, 2021, **1205**, 113445.
34 S. Smidstrup, T. Markussen, P. Vancraeyveld, J. Wellendorff, J. Schneider, T. Gunst, B. Verstichel, D. Stradi, P. A. Khomyakov, U. G. Vej-Hansen, M. E. Lee, S. T. Chill, F. Rasmussen, G. Penazzi, F. Corsetti, A. Ojanperä, K. Jensen, M. L. N. Palsgaard, U. Martinez, A. Blom, M. Brandbyge and K. Stokbro, *J. Phys.: Condens. Matter*, 2019, **32**, 015901.
35 B. Kohnke, C. Kutzner and H. Grubmüller, *J. Chem. Theory Comput.*, 2020, **16**, 6938–6949.
36 E. Lindahl, P. Bjelkmar, P. Larsson, M. A. Cuendet and B. Hess, *J. Chem. Theory Comput.*, 2010, **6**, 459–466.
37 P. B. Johnson and R. W. Christy, *Phys. Rev. B*, 1974, **9**, 5056.
38 D. W. Lynch and W. R. Hunter, *Handbook of Optical Constants of Solids*, 1985, vol. 1, pp. 275–367.
39 P. B. Johnson and R. W. Christy, *Phys. Rev. B*, 1972, **6**, 4370.
40 T. Rouxel, *J. Am. Ceram. Soc.*, 2007, **90**, 3019–3039.
41 J. Lintymer, N. Martin, J. M. Chappé, J. Takadoum and P. Delobelle, *Thin Solid Films*, 2006, **503**, 177–189.
42 C. Durkan, A. Ilie, M. S. M. Saifullah and M. E. Welland, *Appl. Phys. Lett.*, 2002, **80**, 4244–4246.
43 F. Zhu, Z. Xie and Z. Zhang, *AIP Adv.*, 2018, **8**, 35321.
44 J. K. Luo, A. J. Flewitt, S. M. Spearing, N. A. Fleck and W. I. Milne, *Mater. Lett.*, 2004, **58**, 2306–2309.
45 S. U. Jen and T. C. Wu, *Thin Solid Films*, 2005, **492**, 166–172.
46 M. Cattani, M. C. Salvadori, L. L. Melo, A. R. Vaz and I. G. Brown, *Phys. Rev. B*, 2003, **67**, DOI: 10.1103/PHYSREVB.67.153404.
47 S. K. Jha, D. Balakumar and R. Paluchamy, *Int. J. Automot. Mech. Eng.*, 2015, **11**, 2317–2331.
48 H. Mizubayashi, J. Matsuno and H. Tanimoto, *Scr. Mater.*, 1999, **41**, 443–448.
49 J. G. Noel, *IET Circuits Devices Syst.*, 2016, **10**, 156–161.